Matter density distributions and radii from small-angle differential cross sections of proton-nucleus elastic scattering at 0.8 GeV

Y. Huang,[1,2] X. Y. Wu,[3] X. L. Tu,[2,*] Z. P. Li,[4] Y. Kuang,[4] J. T. Zhang,[2] and Z. H. Li[2,5]

[1]*Key Laboratory of Radiation Physics and Technology of the Ministry of Education, Institute of Nuclear Science and Technology, Sichuan University, Chengdu 610064, China*

[2]*Institute of Modern Physics, Chinese Academy of Sciences, Lanzhou 730000, China*

[3]*College of Physics and Communication Electronics, Jiangxi Normal University, Nanchang 330022, China*

[4]*School of Physical Science and Technology, Southwest University, Chongqing 400715, China*

[5]*School of Nuclear Science and Technology, Lanzhou University, Lanzhou 730000, China*

(Received 23 August 2023; accepted 9 November 2023; published 27 November 2023)

We determined the matter density distributions and root-mean-square radii of ^{12,13}C, ^{14}N, ^{20,22}Ne, ^{24,26}Mg, ^{30}Si, ^{40,42,44,48}Ca, ^{46,48}Ti, ^{54}Fe, ^{58,64}Ni, ^{90,92}Zr, ^{116,124}Sn, and ^{208}Pb through fitting the relative and the absolute small-angle differential cross sections of proton-nucleus elastic scattering at 0.8 GeV with the Glauber model, respectively. Compared to the absolute cross section analysis method, the radius systematic errors originating from the absolute cross section normalization factors were obviously reduced by the relative cross section analysis method. In particular, with the obtained matter density of the soft nucleus ^{30}Si, an impact of the dynamical correlations on the diffuse density distribution caused by the deformation mixing configurations was discussed. The theoretical calculations were performed within the framework of the particle-number and angular-momentum projected generator coordinate method (PNAMP + GCM) based on the deformed relativistic mean field plus the Bardeen-Cooper-Schrieffer (RMF + BCS) model.

DOI: 10.1103/PhysRevC.108.054610

I. INTRODUCTION

As one of nuclear fundamental properties, matter (proton + neutron) density distributions are sensitive to nucleon occupation number [1,2], radial wave function [3], and deformation [4,5]. Many efforts, including the calculations beyond the mean field, were made to study such as the density bubble structures in the interior of nuclei [6–10]. Root-mean-square (rms) matter radii R_m characterize the sizes of nuclei, which can be directly determined by the matter density distributions. Since the halo phenomenon of ^{11}Li was observed through its remarkably large matter radius by Tanihata *et al.* [11], large amounts of experiments [12–15] have been carried out to investigate the matter radius evolution. For more contents see review articles [16–19] and references cited therein. Combined with proton distribution radii R_p, neutron distribution radii R_n of nuclei can be extracted from the matter radii. The neutron radii are also essential to search new physics via the atomic parity violation [20] and the coherent elastic neutrino-nucleus scattering experiments [21]. Moreover, the difference of the neutron and proton distribution radii in a nucleus, namely, $\Delta R_{np} = R_n - R_p$, known as neutron skin thickness, plays an important role in constraining the symmetry energy slope L at the saturation density [22,23]. They are also widely applied to constrain the effective interaction parameters of the self-consistent mean field models [24,25].

Because of the importance including but not limited to those mentioned above, precise radius measurements continue to attract much attention. Recently, besides the model-independent parity violation electron scattering experiments [26,27], the in-ring reaction experimental techniques were also developed [28–30]. One aim of the in-ring reaction experiments is to determine the matter density distributions and radii through measuring the small-angle differential cross sections of hadron-nucleus elastic scattering [31–37]. The novel methods were initiated at Gesellschaft für Schwerionenforschung GmbH (GSI) [29]. Such kinds of experiments are operated in inverse kinematics, where stored heavy ions repeatedly interact with an internal gas-jet target in experimental storage ring. These experiments are characterized by windowless target, low momentum detection sensitivity, and low background [28–37]. Recently, a significant core rearrangement effect from ^{56}Ni to ^{58}Ni was found through their matter density difference extracted from the small-angle differential cross sections [31], which were measured by the in-ring reaction facility at the Experimental Storage Ring (ESR) at GSI [33].

The Cooler Storage Ring at the Heavy Ion Research Facility in Lanzhou (HIRFL-CSR) [38] is similar to the heavy ion synchrotron-experimental storage ring facility (SIS-ESR) at GSI [28]. The HIRFL-CSR consists of the main storage ring (CSRm) and the experimental cooler storage ring (CSRe). These two rings are connected by the projectile fragment separator (RIBLL2). The CSRe equipped with the internal gas-jet target [39] and electron cooler [40] also provides an

*tuxiaolin@impcas.ac.cn

opportunity for performing the in-ring proton-nucleus elastic scattering experiments to determine the matter density distributions and radii of nuclei. Experiments of ^{58}Ni$(p, p)^{58}$Ni and ^{78}Kr$(p, p)^{78}$Kr elastic scatterings at low momentum transfer were successfully performed at the HIRFL-CSR [35,36]. For more details for the in-ring reaction facility at the HIRFL-CSR see Refs. [35–37].

Matter density distributions and radii were usually determined by fitting the absolute differential cross sections with suitable reaction models [14,15]. As known, reaction luminosities are essential for determining the absolute cross sections. However, as mentioned by the review article [41], precise measurements of the reaction luminosities are challenging work for the in-ring experiments, since it is difficult to precisely determine gas-target density, beam intensity, and the overlap between the target and beam. The luminosity normalization uncertainty was around 15% for the in-ring ^{56}Ni$(p, p)^{56}$Ni experiment at the ESR [33]. As a result, theoretical atomic cross sections were sometimes adopted to determine the absolute cross sections for the in-ring reaction experiments [35,42,43]. The uncertainty of the absolute cross section normalization would result in large systematic errors for the density distribution and radius measurements. In order to reduce the effects of the absolute normalization, a free cross section normalization parameter, L_0, was introduced to extract matter density distributions and radii through fitting the relative differential cross sections. That is to say, matter densities and radii were determined through comparing the shapes of the experimental and calculated differential cross sections. This relative cross section fit method was employed to extract the matter radii in previous work [2,36,44]. However, the validity and the precision of the relative method are not systematically examined.

In the present work, the matter density distributions and root-mean-square radii of 25 nuclei were extracted through fitting the relative and the absolute differential cross sections with the Glauber model, respectively. The effects of the cross section normalization uncertainties on the matter radii were checked. To study the validity and the precision of the relative method, the radii deduced from the density distributions were compared to the results of the antiprotonic atom x-ray experiments [45]. This is not only important for investigating physics related to the matter radii, but also plays an important role in constructing the in-ring reaction facilities at next-generation heavy-ion storage rings, such as the High Intensity heavy ion Accelerator Facility (HIAF) [46] and the Facility for Antiproton and Ion Research (FAIR) [29]. In particular, with the determined matter density distribution of the soft nucleus ^{30}Si, the impact of the dynamical correlations beyond the mean field on the diffuse surface density distribution was discussed within the framework of particle-number and angular-momentum projected generator coordinate method (PNAMP + GCM) [8].

II. DIFFERENTIAL CROSS SECTIONS

The small-angle differential cross sections of proton-nucleus elastic scattering are from the peripheral collisions. They are sensitive to the matter radii related to the surface

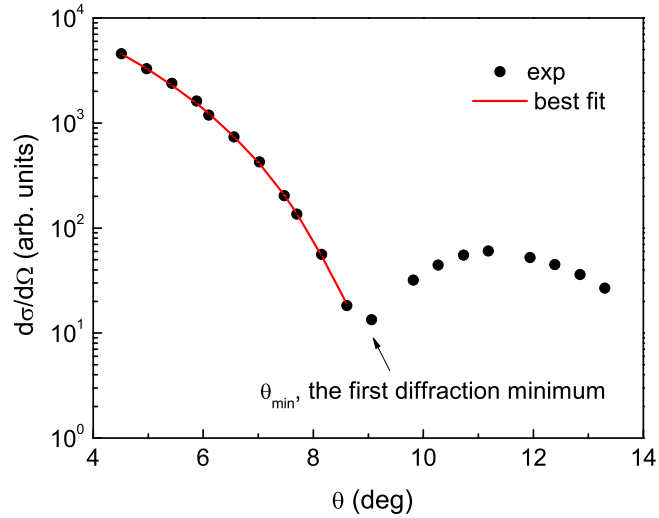

FIG. 1. The best fit of the small-angle differential cross sections as a function of scattering angle θ in the center-of-mass frame for ^{30}Si, which was obtained by the relative cross section analysis method. The experimental cross sections were normalized to the cross sections of the best fit by multiplying L_0.

density distributions. For instance, experiments based on the active gas target [14,47–49] and the internal gas-jet target [31,34–36] were developed to determine the matter radii through measuring the small-angle differential cross sections. In this work, we used the relative and the absolute small-angle differential cross sections to extract the surface matter density distributions and radii of ^{12,13}C, ^{14}N, ^{20,22}Ne, ^{24,26}Mg, ^{30}Si, ^{40,42,44,48}Ca, ^{46,48}Ti, ^{54}Fe, ^{58,64}Ni, ^{90,92}Zr, ^{116,124}Sn, and ^{208}Pb, respectively. The scattering angle smaller than the angle $\theta_{\min}$ at the first diffraction minimum of the differential cross sections was considered as the small angle in this work, see Fig. 1. In the small-angle region, the effects of the spin-orbit can not only be neglected, but the two parameters of the Fermi density distribution can also be constrained simultaneously.

The adopted experimental differential cross sections of ^{12,13}C [50–52], ^{14}N [53], ^{20,22}Ne [54], ^{24,26}Mg [55], ^{30}Si [56], ^{40,42,44,48}Ca [57,58], ^{46,48}Ti [59], ^{54}Fe [60], ^{58,64}Ni [60], ^{90,92}Zr [61,62], ^{116,124}Sn [63], and ^{208}Pb [64] were measured by the high-resolution spectrometer (HRS) at the Clinton P. Anderson Meson Physics Facility (LAMPF) of the Los Alamos Scientific Laboratory. They were used to investigate matter density distributions and optical model parameters, for instance. These data are available in the EXFOR database [65]. A relative statistical error of better than 1% was achieved for the small-angle differential cross sections. However, the uncertainties of the absolute cross sections were around 10% [50,63]. More details on experiments and the HRS can be found in Refs. [66,67].

III. EXTRACTIONS OF MATTER DENSITY DISTRIBUTIONS AND RADII

As known, the matter density distributions can be probed through the differential cross sections of proton-nucleus elastic scattering based on appropriate reaction models. The

Glauber model is one of the well established tools to describe the scattering processes for the intermediate-high energy nucleus-nucleus collisions [68,69]. It was widely applied to extract the matter density distributions and radii of nuclei from the small-angle differential cross sections [2,14,31,33,44,47,48].

In the present work, we also employed a procedure based on the Glauber model [68] to extract the matter density distributions, in which the spin-orbit term was not considered [47]. The differential cross sections of proton-nucleus elastic scattering as a function of scattering angle θ in the center-of-mass frame were calculated in the Glauber model via [47,69]

$$\frac{d\sigma}{d\Omega}(\theta) = \left| f_0(\boldsymbol{q}) + ik \int_0^\infty [e^{i\chi_{0c}} - e^{i\chi_c}(1-\Gamma_{pp})^Z \times (1-\Gamma_{pn})^N] J_0(\boldsymbol{q}b) b db \right|^2,$$

where $f_0(\boldsymbol{q})$ is the standard Coulomb amplitude. The $e^{i\chi_{0c}}$ and $e^{i\chi_c}$ are the Coulomb phases corresponding to the point charge and the folded charge density, respectively.

The matter density distribution $\rho(r)$ and the proton-nucleon scattering amplitude $f_{pj}(\boldsymbol{q})$ are essential input quantities in the profile function $\Gamma_{pj}(b)$ calculations as

$$\Gamma_{pj}(b) = -\frac{i}{k} \int_0^\infty f_{pj}(\boldsymbol{q}) S_j(\boldsymbol{q}) J_0(\boldsymbol{q}b) \boldsymbol{q} d\boldsymbol{q}, \quad (j = n, p),$$

where the form factor $S_j(\boldsymbol{q})$ was obtained by the Fourier transform of the density $\rho(r)$ via

$$S_j(\boldsymbol{q}) = 4\pi \int \rho(r) \frac{\sin(\boldsymbol{q}r)}{\boldsymbol{q}} r dr.$$

The method with the matter density instead of proton and neutron densities in the profile function calculations is not only independent of the electron scattering data, but also does not introduce any significant inaccuracy [70].

Different phenomenological density profiles would result in a slight radius difference [47,48]. In order to compare with the results in Ref. [45], we also assumed that the surface matter density distributions can be described by the two-parameter Fermi (2pF) model as

$$\rho(r) = \rho(0) \frac{1}{1 + \exp\left(\frac{r-R}{a}\right)},$$

where $\rho(0)$, R, and a are the density normalization factor, half-density radius, and diffuseness parameter, respectively.

The spin-orbit effects were known to be negligible in the small-angle region [47,69], thereby, the $f_{pj}(\boldsymbol{q})$ was calculated with less input parameters via

$$f_{pj}(\boldsymbol{q}) = \frac{ik}{4\pi} \sigma_{pj}(1 - i\alpha_{pj}) \exp\left(\frac{-\boldsymbol{q}^2 \beta_{pj}}{2}\right),$$

where σ_{pj}, α_{pj}, and β_{pj} are the total cross sections, ratios of the real to imaginary parts of the forward-scattering amplitudes, and slope parameters for proton-proton (pp) and proton-neutron (pn) channels, respectively. The used values were taken from Ref. [2], where $\sigma_{pp} = 4.70(2)\,\mathrm{fm}^2$, $\sigma_{pn} = 3.80(2)\,\mathrm{fm}^2$, $\alpha_{pp} = -0.02(6)$, $\alpha_{pn} = -0.34(6)$, and $\beta_{pp} = \beta_{pn} = 0.20(5)\,\mathrm{fm}^2$. Otherwise, the center of mass motion was also corrected as Ref. [69] in the cross section calculations.

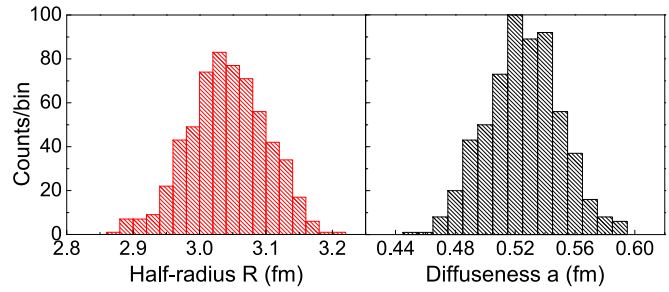

FIG. 2. The distributions of the obtained R and a for ^{30}Si, which were caused by the uncertainties of differential cross sections.

To reduce the effects of the absolute cross section normalization uncertainties, we introduced a free cross section normalization parameter L_0, such that the density distributions were determined by fitting the relative differential cross sections. Therefore, in the χ^2 procedure of the least square fit, the half-density radius R, diffuseness parameter a, and normalization parameter L_0 were freely adjusted to fit the small-angle differential cross sections. The χ^2 function is defined as

$$\chi^2 = \sum_i^{N_0} \frac{\left[L_0 \frac{d\sigma}{d\Omega}(\theta_i)_{\mathrm{exp}} - \frac{d\sigma}{d\Omega}(\theta_i)_{\mathrm{cal}}\right]^2}{\left[L_0 \Delta \frac{d\sigma}{d\Omega}(\theta_i)_{\mathrm{exp}}\right]^2},$$

where N_0, $\frac{d\sigma}{d\Omega}(\theta)_{\mathrm{exp}}$, and $\Delta\frac{d\sigma}{d\Omega}(\theta)_{\mathrm{exp}}$ are the number of data points, reported absolute differential cross sections, and cross section errors, respectively. The $\frac{d\sigma}{d\Omega}(\theta)_{\mathrm{cal}}$ are the calculated differential cross sections by the Glauber model. Subsequently, the rms point-matter radii R_m were calculated by the obtained R and a via

$$R_m = \left(\frac{\int \rho(r) r^4 dr}{\int \rho(r) r^2 dr}\right)^{\frac{1}{2}}.$$

The best fit of the small-angle differential cross sections for ^{30}Si obtained by the relative analysis method, as an example, is shown in Fig. 1.

The tabulated uncertainties of differential cross sections would result in different fit values for R, a, and L_0. Figure 2 shows the distributions of the obtained R and a for ^{30}Si. They were obtained by fitting hundreds of randomly sampling differential cross sections based on the Gaussian distribution within $\frac{d\sigma}{d\Omega}(\theta_i)_{\mathrm{exp}} \pm 2\Delta\frac{d\sigma}{d\Omega}(\theta_i)_{\mathrm{exp}}$. The standard deviations of these distributions were considered as the statistical errors of the corresponding data. Note that the used experimental errors $\Delta\frac{d\sigma}{d\Omega}(\theta_i)_{\mathrm{exp}}$ were proportionally scaled to make the normalized χ_n of the best fit equal 1. Table I summarizes the L_0, R, a, and R_m^{rel} obtained by the relative cross section analysis method.

To demonstrate an advantage of the relative analysis method, the matter radii R_m^{abs} were also determined by fitting the absolute differential cross sections, that is to say, the L_0 was fixed to be 1 in the χ^2 function, and the R and a were free parameters. Furthermore, some observables cannot constrain

TABLE I. The obtained cross section normalization factor L_0, half-density radius R, diffuseness parameter a, and rms point-matter radii R_m in the present work. $R_m^{\rm rel}$ are the matter radii obtained by fitting the relative differential cross sections, where L_0, R, and a were free parameters. The L_0, R, a, and $R_m^{\rm rel}$ for ^{20,22}Ne, ^{24,26}Mg, and ^{90,92}Zr were taken from Refs. [2,75], respectively, which were obtained with the same method. R_m^{a55} and R_m^{a50} are the matter radii obtained by fitting the relative differential cross sections, where L_0 and R were free parameters, but a was fixed to be 0.55 fm and 0.50 fm, respectively. R_m^{abs} are the matter radii obtained by fitting the absolute differential cross sections, namely, L_0 was fixed to be 1, and R and a were adjusted to fit. The matter radii $R_m^{\rm lit}$ were deduced by the linear relationship in Ref. [45]. $a_{ch}^{\rm exp}$ are the experimental diffuseness parameters for the 2pF charge distributions, which were taken from Ref. [76]. The R, a, and R_m are shown in units of fm. The errors in parentheses are only statistical uncertainties. The systematical error is about 0.030 fm.

Nuclei	L_0	R	a	$a_{ch}^{\rm exp}$ [76]	$R_m^{\rm rel}$ (free L_0, R, a)	R_m^{a55} ($a = 0.55$)	R_m^{a50} ($a = 0.50$)	R_m^{abs} ($L_0 = 1$)	$R_m^{\rm lit}$ [45]
^{12}C	1.147(6)	2.090(26)	0.430(9)		2.275(10)	2.428	2.356	2.461	2.307
^{12}C	1.110(8)	1.995(26)	0.480(8)		2.360(11)	2.458	2.387	2.503	2.307
^{13}C	1.172(8)	1.995(30)	0.485(9)		2.374(12)	2.464	2.394	2.614	2.342
^{14}N	1.235(27)	1.990(51)	0.505(17)		2.428(25)	2.497	2.421	2.674	2.400
^{20}Ne	1.250(78)	2.422(67)	0.592(30)	0.571	2.891(52) [2]	2.821	2.749	3.081	2.869
^{22}Ne	1.455(152)	2.396(170)	0.598(66)	0.549	2.895(104) [2]	2.824	2.760	3.291	2.866
^{24}Mg	1.045(17)	2.860(55)	0.518(21)	0.551	2.935(20) [2]	2.966	2.918	2.990	2.922
^{26}Mg	0.998(18)	2.904(57)	0.512(22)	0.523	2.946(21) [2]	2.983	2.936	2.945	2.941
^{30}Si[a]	0.935(22)	3.055(58)	0.520(25)		3.055(24)	3.086	3.036	3.000	3.039
^{40}Ca	0.986(10)	3.765(41)	0.435(21)		3.335(10)	3.402	3.371	3.322	3.357
^{40}Ca	1.017(10)	3.765(40)	0.450(19)		3.362(11)	3.420	3.387	3.379	3.357
^{42}Ca	1.014(6)	3.655(30)	0.500(13)		3.387(7)	3.417	3.387	3.398	3.414
^{44}Ca	1.028(16)	3.625(101)	0.525(39)		3.419(21)	3.433	3.406	3.452	3.450
^{48}Ca	0.922(52)	3.735(79)	0.520(40)		3.479(40)	3.505	3.462	3.426	3.459
^{46}Ti	1.020(21)	3.615(56)	0.570(24)		3.511(21)	3.495	3.458	3.532	3.514
^{48}Ti	0.990(28)	3.745(73)	0.530(35)	0.588	3.507(27)	3.520	3.484	3.499	3.522
^{54}Fe	0.975(6)	4.145(22)	0.415(12)	0.536	3.562(6)	3.619	3.593	3.543	3.599
^{58}Ni	1.017(7)	4.015(49)	0.530(19)		3.681(9)	3.689	3.670	3.697	3.682
^{64}Ni	1.280(33)	4.350(82)	0.415(45)	0.578	3.706(20)	3.764	3.737	3.958	3.820
^{90}Zr	1.114(7)	4.610(47)	0.580(19)		4.171(10)	4.165	4.153	4.323	4.232
^{90}Zr	0.900(5)	4.745(44)	0.565(17)		4.233(6) [75]	4.230	4.223	4.181	4.232
^{92}Zr	0.934(9)	4.835(93)	0.580(37)		4.321(11) [75]	4.315	4.310	4.284	4.281
^{116}Sn	0.998(8)	5.365(85)	0.560(37)	0.550	4.648(10)	4.649	4.644	4.649	4.611
^{124}Sn	1.229(19)	5.715(140)	0.505(70)	0.534	4.808(19)	4.813	4.808	5.195	4.699
^{208}Pb	1.007(10)	6.635(61)	0.530(33)		5.504(21)	5.506	5.502	5.514	5.550

[a]Systematic trend indicates that the tabulated cross sections of ^{30}Si in the EXFOR [65] would be also in the center-of-mass system as other nuclei.

the R and a simultaneously. For instance, either R or a needs to be fixed for extracting matter radii through the interaction cross section [12,71]. Similar situations may also exist for the in-ring elastic scattering experiments, if the measured angular ranges are too small [36]. Therefore, we also extracted the matter radii R_m^{a50} and R_m^{a55}, where the a was respectively fixed to be 0.50 fm [71] and 0.55 fm [12], and only the R and L_0 as free parameters were adjusted to fit. The obtained R_m^{abs}, R_m^{a50}, and R_m^{a55} are also tabulated in Table I.

IV. DISCUSSION

A. Validity and precision of the relative analysis method

Due to poor knowledge of the strong interactions, most of the matter radius measurements are model-dependent. The model-independent matter radius data are scarce, although remarkable progresses were made by the parity violation electron scattering experiments [26,27]. The neutron skin thicknesses ΔR_{np} of stable nuclei in the $\delta = (N - Z)/A$ range from 0 to about 0.23 were determined by the antiprotonic atom x-ray experiments [45], where N, Z, and A are the neutron, proton, and mass numbers, respectively. According to these ΔR_{np} data, a linear relationship between ΔR_{np} and δ, namely, $\Delta R_{np} = (-0.04 \pm 0.03) + (1.01 \pm 0.15)\delta$, was obtained [45]. Especially, the evaluated ΔR_{np} based on various experiments [72] can be reproduced within about 0.03 fm by the linear relationship [45]. Thus, for the sake of simplicity, to estimate the validity and the precision of the relative analysis method, our results were compared to the radii obtained by the linear relationship [45], see Table I.

Charge radii related to the well-known electromagnetic interactions have been precisely measured [73]. By taking into account the main corrections, the point-proton distribution radii of nuclei were deduced from the charge radii via $R_p^2 = R_{ch}^2 - r_p^2 - \frac{N}{Z} r_n^2 - \frac{3\hbar^2}{4m_p^2c^2}$ [74], where R_{ch}, r_p, and r_n^2 are the charge radius, proton charge radius, and neutron squared charge radius, respectively. They are available in Ref. [73]. The Darwin-Foldy correction factor $\frac{3\hbar^2}{4m_p^2c^2}$ was 0.033 fm^2 [74]. Combined with the ΔR_{np} determined by the antiprotonic atom x-ray experiments [45], the point-neutron distribution radii of nuclei were obtained through $R_n = R_p + \Delta R_{np}$. Subsequently,

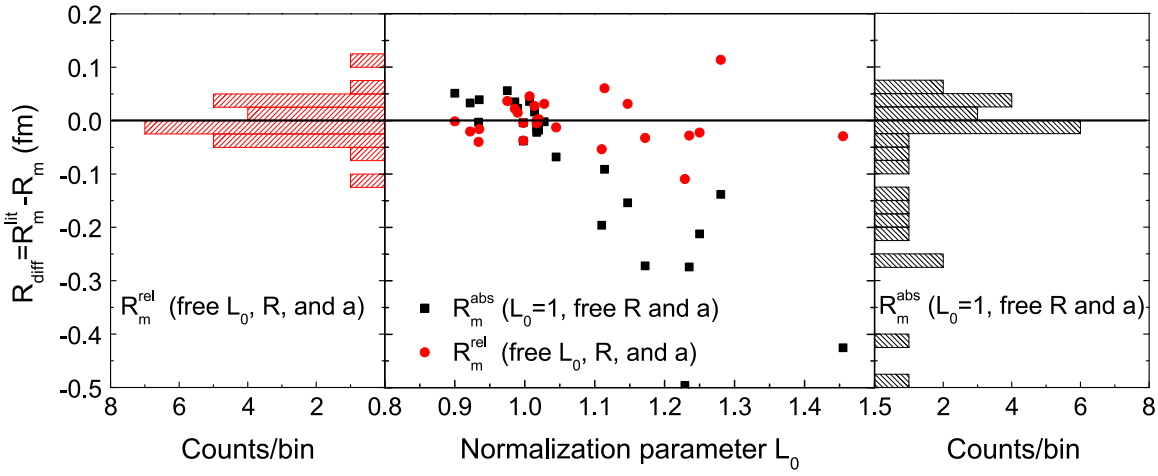

FIG. 3. Comparison of our results ($R_m^{\rm rel}$, R_m^{abs}) and the $R_m^{\rm lit}$, the latter was deduced from the antiprotonic atom x-ray experiments [45]. A radius systematic deviation from the absolute differential cross sections fit can be effectively reduced by using the relative cross section fit method.

see Table I, the reference matter radii $R_m^{\rm lit}$ were calculated via $R_m^{\rm lit} = (\frac{N}{A}R_n^2 + \frac{Z}{A}R_p^2)^{1/2}$.

As shown in Table I, although most of the obtained normalization factors L_0 in this work are close to the expected value of 1, there are still about 10–40 % differences for ^{12,13}C, ^{14}N, ^{20,22}Ne, ^{64}Ni, ^{90}Zr, and ^{124}Sn. Figure 3 demonstrates the comparisons of our radii and $R_m^{\rm lit}$. We can see that there is an obvious systematic deviation in the L_0 range from about 1.1 to 1.5 for the R_m^{abs} obtained by fitting the absolute cross sections. This suggests that the cross section normalization deviations would introduce large systematic errors for the radius determinations. If the deduced radii $R_m^{\rm lit}$ [45] are reliable, as shown in Fig. 3, the relative cross section method effectively reduces the systematic errors of radii, compared to the absolute cross section fit method. The mean value for the difference, $R_{\rm diff} = R_m^{\rm lit} - R_m^{\rm rel}$, is about -0.001 fm. It is very close to the expected value of 0 fm. The spread of the $R_{\rm diff}$ for the 25 nuclei is about 0.040 fm. Especially, for the ^{12}C, ^{14}N, ^{20}Ne, ^{24}Mg, and ^{40}Ca nuclei, which have the same proton and neutron numbers, where the matter radii are expected to be approximately equal to the corresponding proton radii. This is almost model-independent. Compared to these proton radii R_p, an average difference of 0.010 fm was obtained for $R_m^{\rm rel}$. The standard deviation for the difference between R_p and $R_m^{\rm rel}$ is about 0.030 fm, which can be considered as a systematical error. These results suggest that the relative analysis method gives reliable radii, and effectively reduces systematic errors.

Moreover, as shown in the insert of Fig. 4, both R_m^{a55} and R_m^{a50} are very consistent with the $R_m^{\rm rel}$ for the medium-heavy nuclei with $A \geqslant 40$. Their spreads are less than about 0.02 fm for the medium-heavy nuclei with $A \geqslant 40$, see Fig. 4. Especially, most of the obtained a in this work are close to the diffuseness parameter $a_{ch}^{\rm exp}$ of the 2pF charge distributions [76]. Thus, it is reasonable to extract matter radii through fixing the a to be the values from the charge density distributions [71].

B. Matter density distribution of ^{30}Si

Theoretically, the self-consistent mean field approaches have been proved as powerful tools for describing ground-state properties of nuclei [77]. In order to further describe energy spectra and transition probabilities, some correlations beyond the mean field need to be considered [25,77]. Recently, the density bubble structures were investigated by considering the correlations beyond the mean field [6–9].

The matter density distributions in this work were extracted from the small-angle differential cross sections related to the peripheral collisions. As a result, only surface density distributions were precisely determined. ^{30}Si is a nucleus with a soft potential-energy surface [78]. Due to a large fluctuation in the quadrupole shape degree of freedom, the deformation mixing

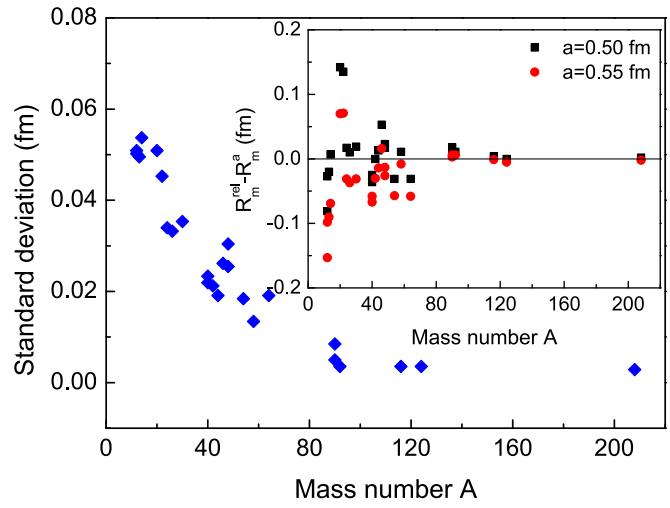

FIG. 4. The standard deviations of the matter radii R_m^{a50} and R_m^{a55}, which were obtained by fixing the a to be 0.50 fm and 0.55 fm, respectively. The insert shows the matter radius differences for R_m^{a50} and R_m^{a55}, which were compared to the $R_m^{\rm rel}$, respectively.

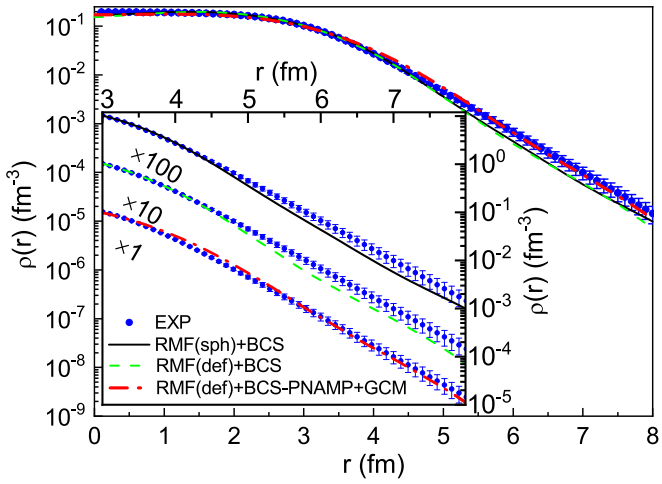

FIG. 5. Comparison of the experimental and calculated matter density distributions for the soft nucleus ^{30}Si. Theoretical densities were calculated by the spherical RMF + BCS (black solid line), the deformed RMF + BCS (green dashed line), and the PNAMP + GCM based on the deformed RMF + BCS models (red dash-dotted line), respectively. The dynamical correlations beyond the mean field were considered by the PNAMP + GCM method. The densities in the insert are shifted to clearly show the tail details.

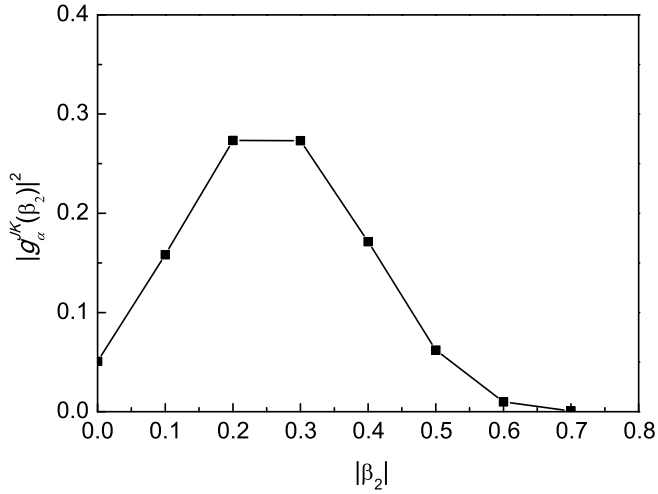

FIG. 6. The square of collective wave functions $|g_\alpha^{JK}(\beta_2)|^2$ as a function of deformation parameter β_2 for the ^{30}Si ground state, which was obtained by using the PNAMP + GCM method based on the deformed RMF + BCS. Lines connecting data points are only guides for the eye.

configurations are expected in ^{30}Si. The beyond mean field calculations have already been used to study the deformation difference between the hypernucleus $^{30}_{\Lambda}$Si and the original nucleus ^{30}Si [78]. In this work, it provides an opportunity to test the effects of the dynamical correlations beyond the mean field on the surface matter density distribution of the soft nucleus ^{30}Si.

First, we employed the spherical relativistic mean field plus the Bardeen-Cooper-Schrieffer (RMF + BCS) model to calculate the matter density distribution of ^{30}Si. The PC-PK1 density functional [79] was utilized in all calculations. In Fig. 5, it can be observed that the experimental surface density distribution is more diffuse, and is systematically larger than the theoretical one calculated by the spherical RMF + BCS within a range of $r = 4.5$–8 fm. Furthermore, we used the deformed RMF + BCS to analyze the data, and it gives a global minimum with quadrupole deformation parameter $\beta_2 \sim 0.1$. This positive β_2 is consistent with the conclusion of prolate shape for ^{30}Si [80,81]. However, the obtained space-angle-averaged density (dashed line) still underestimates the diffuse experimental density distribution, see Fig. 5.

Theoretical calculations have already shown that the dynamical correlations have important impacts on inner density distributions, especially for the soft nuclei [8]. These dynamical correlations mainly include the restoration of rotational symmetry for the intrinsic quadrupole deformed states and the fluctuation in the quadrupole shape degree of freedom. To study the effects of the dynamical correlations in this work, the density distribution of ^{30}Si was calculated within the framework of the particle-number and angular-momentum projected generator coordinate method (PNAMP + GCM) based on the deformed RMF + BCS [7,8]. Figure 6 shows the square of collective wave functions $|g_\alpha^{JK}(\beta_2)|^2$ as a function of the deformation parameters β_2 for the ground state of ^{30}Si. We can see that the deformation parameter $|\beta_2|$ of about 0.3 at maximum probability is consistent with the experimental value of 0.31 [82]. Especially, the spread of β_2 is very large, and there are significant deformation mixing configurations for the soft nucleus ^{30}Si. The density distribution extracted from these deformation mixing configurations reproduces the diffuse tail density distribution for the soft nucleus ^{30}Si, as shown in Fig. 5. We note that the calculated matter radius of 3.14 fm is larger than the experimental value of $3.055(24)_{sta}(30)_{sys}$ fm. This could be because the PC-PK1 functional was obtained by fitting to the experimental charge radii in the mean field level [79]. These results suggest that the dynamical correlations beyond the mean field play an important role in describing the diffuse surface matter distributions of soft nuclei caused by the large deformation mixing configurations.

V. SUMMARY

Matter density distributions and radii of ^{12,13}C, ^{14}N, ^{20,22}Ne, ^{24,26}Mg, ^{30}Si, ^{40,42,44,48}Ca, ^{46,48}Ti, ^{54}Fe, ^{58,64}Ni, ^{90,92}Zr, ^{116,124}Sn, and ^{208}Pb were extracted from the reported small-angle differential cross sections by using the relative and the absolute cross section analysis methods based on the Glauber model, respectively. The matter radii obtained by the relative cross section method are consistent with the results of the antiprotonic atom x-ray experiments within a standard deviation of about 0.04 fm. The systematic errors of radii depending on the cross section normalization factors were obviously reduced by the relative analysis method.

Furthermore, the impact of the dynamical correlations beyond the mean field was tested by the obtained surface matter density distribution of the soft nucleus ^{30}Si. Compared to

the spherical and the deformed RMF + BCS model calculations, the diffuse tail density distribution of ^{30}Si resulted by the deformation mixing configurations was described by considering the dynamical correlations within the framework of the PNAMP + GCM based on the deformed RMF + BCS model.

ACKNOWLEDGMENTS

This work is supported in part by the NSFC (Grants No. 12022504, No. 12121005, No. 12375115, and No. 12005082) and the CAS Open Research Project of large research infrastructures.

[1] A. Mutschler, A. Lemasson, O. Sorlin, D. Bazin, C. Borcea, R. Borcea, Z. Dombrádi, J.-P. Ebran, A. Gade, H. Iwasaki *et al.*, Nat. Phys. **13**, 152 (2017).

[2] Z. H. Li, Y. Kuang, Y. Huang, X. L. Tu, Z. P. Li, K. H. Fang, J. T. Zhang, and K. Yue, Phys. Rev. C **107**, 064310 (2023).

[3] J. M. Cavedon, B. Frois, D. Goutte, M. Huet, P. Leconte, C. N. Papanicolas, X. H. Phan, S. K. Platchkov, S. Williamson, W. Boeglin, and I. Sick, Phys. Rev. Lett. **49**, 978 (1982).

[4] S. Watanabe, K. Minomo, M. Shimada, S. Tagami, M. Kimura, M. Takechi, M. Fukuda, D. Nishimura, T. Suzuki, T. Matsumoto *et al.*, Phys. Rev. C **89**, 044610 (2014).

[5] W. Horiuchi and T. Inakura, Prog. Theor. Exp. Phys. **2021**, 103D02 (2021).

[6] J. M. Yao, S. Baroni, M. Bender, and P. H. Heenen, Phys. Rev. C **86**, 014310 (2012).

[7] J. M. Yao, H. Mei, and Z. P. Li, Phys. Lett. B **723**, 459 (2013).

[8] X. Y. Wu, J. M. Yao, and Z. P. Li, Phys. Rev. C **89**, 017304 (2014).

[9] X. Y. Wu and J. Xiang, Phys. Rev. C **98**, 054319 (2018).

[10] H. A. Wilson, Phys. Rev. **69**, 538 (1946).

[11] I. Tanihata, H. Hamagaki, O. Hashimoto, Y. Shida, N. Yoshikawa, K. Sugimoto, O. Yamakawa, T. Kobayashi, and N. Takahashi, Phys. Rev. Lett. **55**, 2676 (1985).

[12] T. Suzuki, H. Geissel, O. Bochkarev, L. Chulkov, M. Golovkov, D. Hirata, H. Irnich, Z. Janas, H. Keller, T. Kobayashi *et al.*, Phys. Rev. Lett. **75**, 3241 (1995).

[13] M. Tanaka, M. Takechi, A. Homma, M. Fukuda, D. Nishimura, T. Suzuki, Y. Tanaka, T. Moriguchi, D. S. Ahn, A. Aimaganbetov *et al.*, Phys. Rev. Lett. **124**, 102501 (2020).

[14] G. D. Alkhazov, M. N. Andronenko, A. V. Dobrovolsky, P. Egelhof, G. E. Gavrilov, H. Geissel, H. Irnich, A. V. Khanzadeev, G. A. Korolev, A. A. Lobodenko *et al.*, Phys. Rev. Lett. **78**, 2313 (1997).

[15] S. Terashima, H. Sakaguchi, H. Takeda, T. Ishikawa, M. Itoh, T. Kawabata, T. Murakami, M. Uchida, Y. Yasuda, M. Yosoi *et al.*, Phys. Rev. C **77**, 024317 (2008).

[16] I. Tanihata, H. Savajols, and R. Kanungo, Prog. Part. Nucl. Phys. **68**, 215 (2013).

[17] H. Sakaguchi and J. Zenihiro, Prog. Part. Nucl. Phys. **97**, 1 (2017).

[18] G. D. Alkhazov, I. S. Novikov, and Y. M. Shabelski, Int. J. Mod. Phys. E **20**, 583 (2011).

[19] P. Egelhof, Prog. Part. Nucl. Phys. **46**, 307 (2001).

[20] A. Derevianko, Phys. Rev. Lett. **85**, 1618 (2000).

[21] M. Cadeddu, C. Giunti, Y. F. Li, and Y. Y. Zhang, Phys. Rev. Lett. **120**, 072501 (2018).

[22] L. W. Chen, C. M. Ko, B. A. Li, and J. Xu, Phys. Rev. C **82**, 024321 (2010).

[23] B. A. Li, L. W. Chen, and C. M. Ko, Phys. Rep. **464**, 113 (2008).

[24] T. Nikšić, D. Vretenar, P. Finelli, and P. Ring, Phys. Rev. C **66**, 024306 (2002).

[25] T. Nikšić, D. Vretenar, and P. Ring, Prog. Part. Nucl. Phys. **66**, 519 (2011).

[26] D. Adhikari, H. Albataineh, D. Androic, K. Aniol, D. S. Armstrong, T. Averett, C. Ayerbe Gayoso, S. Barcus, V. Bellini, R. S. Beminiwattha *et al.*, Phys. Rev. Lett. **126**, 172502 (2021).

[27] D. Adhikari, H. Albataineh, D. Androic, K. A. Aniol, D. S. Armstrong, T. Averett, C. Ayerbe Gayoso, S. K. Barcus, V. Bellini, R. S. Beminiwattha *et al.*, Phys. Rev. Lett. **129**, 042501 (2022).

[28] M. Steck and Y. A. Litvinov, Prog. Part. Nucl. Phys. **115**, 103811 (2020).

[29] H. H. Gutbrod, I. Augustin, H. Eickhoff, K.-D. Gross, W. F. Henning, D. Krämer, and G. Walter, FAIR Baseline Technical Report, GSI Helmholtzzentrum für Schwerionenforschung, Darmstadt, No. GSI-2013-04788 (2006).

[30] J. Glorius and C. G. Bruno, Eur. Phys. J. A **59**, 81 (2023).

[31] X. Liu, P. Egelhof, O. Kiselev, and M. Mutterer, Phys. Lett. B **809**, 135776 (2020).

[32] P. Egelhof, JPS Conf. Proc. **35**, 011002 (2021).

[33] M. von Schmid, T. Aumann, S. Bagchi, S. Bönig, M. Csatlós, I. Dillmann, C. Dimopoulou, P. Egelhof, V. Eremin, T. Furuno *et al.*, Eur. Phys. J. A **59**, 83 (2023).

[34] J. C. Zamora, T. Aumann, S. Bagchi, S. Bönig, M. Csatlós, I. Dillmann, C. Dimopoulou, P. Egelhof, V. Eremin, T. Furuno *et al.*, Phys. Rev. C **96**, 034617 (2017).

[35] K. Yue, J. T. Zhang, X. L. Tu, C. J. Shao, H. X. Li, P. Ma, B. Mei, X. C. Chen, Y. Y. Yang, X. Q. Liu *et al.*, Phys. Rev. C **100**, 054609 (2019).

[36] J. T. Zhang, P. Ma, Y. Huang, X. L. Tu, P. Sarriguren, Z. P. Li, Y. Kuang, W. Horiuchi, T. Inakura, L. Xayavong *et al.*, Phys. Rev. C **108**, 014614 (2023).

[37] J. T. Zhang, K. Yue, H. X. Li, X. L. Tu, C. J. Shao, P. Ma, B. Mei, X. C. Chen, Y. Y. Yang, X. Q. Liu *et al.*, Nucl. Instrum. Methods Phys. Res. A **948**, 162848 (2019).

[38] J. W. Xia, W. L. Zhan, B. W. Wei, Y. J. Yuan, M. T. Song, W. Z. Zhang, X. D. Yang, P. Yuan, D. Q. Gao, H. W. Zhao *et al.*, Nucl. Instrum. Methods Phys. Res. A **488**, 11 (2002).

[39] C. J. Shao, R. C. Lu, X. H. Cai, D. Y. Yu, F. F. Ruan, Y. L. Xue, J. M. Zhang, D. K. Torpokov, and D. Nikolenko, Nucl. Instrum. Methods Phys. Res. B **317**, 617 (2013).

[40] L. J. Mao, H. Zhao, X. D. Yang, J. Li, J. C. Yang, Y. J. Yuan, V. V. Parkhomchuk, V. B. Reva, X. M. Ma, T. L. Yan *et al.*, Nucl. Instrum. Methods Phys. Res. A **808**, 29 (2016).

[41] J. Eichler and T. Stöhlker, Phys. Rep. **439**, 1 (2007).

[42] J. Glorius, C. Langer, Z. Slavkovská, L. Bott, C. Brandau, B. Brückner, K. Blaum, X. Chen, S. Dababneh, T. Davinson *et al.*, Phys. Rev. Lett. **122**, 092701 (2019).

[43] B. Mei, T. Aumann, S. Bishop, K. Blaum, K. Boretzky, F. Bosch, C. Brandau, H. Bräuning, T. Davinson, I. Dillmann, C. Dimopoulou, O. Ershova, Z. Fulop, H. Geissel, J. Glorius, G. Gyurky, M. Heil, F. Kappeler, A. Kelic-Heil, C.

Kozhuharov, C. Langer, T. LeBleis, Y. Litvinov, G. Lotay, J. Marganiec, G. Munzenberg, F. Nolden, N. Petridis, R. Plag, U. Popp, G. Rastrepina, R. Reifarth, B. Riese, C. Rigollet, C. Scheidenberger, H. Simon, K. Sonnabend, M. Steck, T. Stohlker, T. Szucs, K. Summerer, G. Weber, H. Weick, D. Winters, N. Winters, P. Woods, and Q. Zhong, Phys. Rev. C **92**, 035803 (2015).

[44] Y. Huang, J. T. Zhang, Y. Kuang, J. Geng, X. L. Tu, K. Yue, W. H. Long, and Z. P. Li, Eur. Phys. J. A **59**, 4 (2023).

[45] A. Trzcińska, J. Jastrzębski, P. Lubiński, F. J. Hartmann, R. Schmidt, T. von Egidy, and B. Kłos, Phys. Rev. Lett. **87**, 082501 (2001).

[46] X. H. Zhou and J. C. Yang, AAPPS Bull. **32**, 35 (2022).

[47] G. D. Alkhazov, A. V. Dobrovolsky, P. Egelhof, H. Geissel, H. Irnich, A. V. Khanzadeev, G. A. Korolev, A. A. Lobodenko, G. Münzenberg, M. Mutterer *et al.*, Nucl. Phys. A **712**, 269 (2002).

[48] A. V. Dobrovolsky, G. A. Korolev, S. Tang, G. D. Alkhazov, G. Colò, I. Dillmann, P. Egelhof, A. Estradé, F. Farinon, H. Geissel *et al.*, Nucl. Phys. A **1008**, 122154 (2021).

[49] G. A. Korolev, A. V. Dobrovolsky, A. G. Inglessi, G. D. Alkhazov, P. Egelhof, A. Estradé, I. Dillmann, F. Farinon, H. Geissel, S. Ilieva *et al.*, Phys. Lett. B **780**, 200 (2018).

[50] G. S. Blanpied, W. R. Coker, R. P. Liljestrand, G. W. Hoffmann, L. Ray, D. Madland, C. L. Morris, J. C. Pratt, J. E. Spencer, H. A. Thiessen *et al.*, Phys. Rev. C **18**, 1436 (1978).

[51] G. S. Blanpied, G. W. Hoffmann, M. L. Barlett, J. A. McGill, S. J. Greene, L. Ray, O. B. Van Dyck, J. Amann, and H. A. Thiessen, Phys. Rev. C **23**, 2599 (1981).

[52] G. S. Blanpied, B. G. Ritchie, M. L. Barlett, G. W. Hoffmann, J. A. McGill, M. A. Franey, and M. Gazzaly, Phys. Rev. C **32**, 2152 (1985).

[53] G. S. Blanpied, M. L. Barlett, G. W. Hoffmann, and J. A. McGill, Phys. Rev. C **25**, 2550 (1982).

[54] G. S. Blanpied, B. G. Ritchie, M. L. Barlett, R. W. Fergerson, G. W. Hoffmann, J. A. McGill, and B. H. Wildenthal, Phys. Rev. C **38**, 2180 (1988).

[55] G. S. Blanpied, B. G. Ritchie, M. L. Barlett, G. W. Hoffmann, J. A. McGill, E. C. Milner, K. W. Jones, S. K. Nanda, and R. de Swiniarski, Phys. Rev. C **37**, 1987 (1988).

[56] A. M. Bernstein, R. A. Miskimen, B. Quinn, S. A. Wood, M. V. Hynes, G. S. Blanpied, B. G. Ritchie, and V. R. Brown, Phys. Rev. Lett. **49**, 451 (1982).

[57] L. Ray, G. W. Hoffmann, M. Barlett, J. McGill, J. Amann, G. Adams, G. Pauletta, M. Gazzaly, and G. S. Blanpied, Phys. Rev. C **23**, 828 (1981).

[58] E. Bleszynski, M. Bleszynski, S. Hajisaeid, G. J. Igo, F. Irom, J. B. McClelland, G. Pauletta, A. Rahbar, A. T. M. Wang, C. A. Whitten *et al.*, Phys. Rev. C **25**, 2563 (1982).

[59] G. Pauletta, G. Adams, M. M. Gazzaly, G. J. Igo, A. T. M. Wang, A. Rahbar, A. Wriekat, L. Ray, G. W. Hoffmann, M. Barlett *et al.*, Phys. Lett. B **106**, 470 (1981).

[60] G. W. Hoffmann Jr., G. S. Blanpied, W. R. Coker, C. Harvey, R. P. Liljestrand, G. S. Adams, T. S. Bauer, G. Igo, G. Pauletta, C. A. Whitten, Jr. *et al.*, Phys. Lett. B **79**, 376 (1978).

[61] F. T. Baker, A. Scott, M. A. Grimm, W. G. Love, V. Penumetcha, C. Glashausser, G. S. Adams, G. Igo, G. W. Hoffmann, J. M. Moss *et al.*, Nucl. Phys. A **393**, 283 (1983).

[62] G. W. Hoffman, G. S. Blanpied, W. R. Coker, R. P. Liljestrand, N. M. Hintz, M. A. Oothoudt, T. S. Bauer, G. Igo, G. Pauletta, J. Soukup *et al.*, Phys. Rev. Lett. **40**, 1256 (1978).

[63] G. W. Hoffmann, Jr., G. S. Blanpied, W. R. Coker, R. P. Liljestrand, L. Ray, J. E. Spencer, H. A. Thiessen, N. M. Hintz, M. A. Oothoudt, T. S. Bauer *et al.*, Phys. Lett. B **76**, 383 (1978).

[64] G. W. Hoffmann, L. Ray, M. Barlett, J. McGill, G. S. Adams, G. J. Igo, F. Irom, A. T. M. Wang, C. A. Whitten, Jr., R. L. Boudrie *et al.*, Phys. Rev. C **21**, 1488 (1980).

[65] V. V. Zerkin and B. Pritychenko, Nucl. Instrum. Methods Phys. Res. A **888**, 31 (2018); https://www.nndc.bnl.gov/exfor/.

[66] G. S. Blanpied, W. R. Coker, R. P. Liljestrand, L. Ray, G. W. Hoffman, D. Madland, C. L. Morris, J. C. Pratt, J. E. Spencer, H. A. Thiessen, N. M. Hintz, G. S. Kyle, M. A. Oothoudt, T. S. Bauer, J. C. Fong, G. Igo, R. J. Ridge, C. A. Whitten, T. Kozlowski, D. K. McDaniels, P. Varghese, P. M. Lang, H. Nann, K. K. Seth, and C. Glashausser, Phys. Rev. Lett. **39**, 1447 (1977).

[67] G. W. Hoffmann, D. Madland, C. L. Morris, J. Pratt, J. E. Spencer, N. Tanaka, H. A. Thiessen, B. Zeidman, T. Kozlowski, H. Palevsky *et al.*, AIP Conf. Proc. **41**, 547 (1978).

[68] R. J. Glauber, in *Lectures in Theoretical Physics*, edited by W. E. Brittin and L. G. Dunham (Interscience, New York, 1959), Vol. 1, p. 315.

[69] G. D. Alkhazov, S. L. Belostotsky, and A. A. Vorobyov, Phys. Rep. **42**, 89 (1978).

[70] G. D. Alkhazov, S. L. Belostotsky, O. A. Domchenkov, Y. V. Dotsenko, N. P. Kuropatkin, M. A. Schuvaev, and A. A. Vorobyov, Phys. Lett. B **57**, 47 (1975).

[71] A. Ozawa, T. Baumann, L. Chulkov, D. Cortina, U. Datta, J. Fernandez, H. Geissel, F. Hammache, K. Itahashi, M. Ivanov *et al.*, Nucl. Phys. A **709**, 60 (2002).

[72] J. T. Zhang, X. L. Tu, P. Sarriguren, K. Yue, Q. Zeng, Z. Y. Sun, M. Wang, Y. H. Zhang, X. H. Zhou, and Y. A. Litvinov, Phys. Rev. C **104**, 034303 (2021).

[73] I. Angeli and K. P. Marinova, At. Data Nucl. Data Tables **99**, 69 (2013).

[74] A. Ong, J. C. Berengut, and V. V. Flambaum, Phys. Rev. C **82**, 014320 (2010).

[75] Y. Huang, L. Xayavong, X. L. Tu, J. Geng, Z. P. Li, J. T. Zhang, and Z. H. Li, Phys. Lett. B **847**, 138293 (2023).

[76] H. De Vries, C. W. De jager, and C. De Vries, At. Data Nucl. Data Tables **36**, 495 (1987).

[77] M. Bender, P. H. Heenen, and P. G. Reinhard, Rev. Mod. Phys. **75**, 121 (2003).

[78] H. Mei, K. Hagino, J. M. Yao, and T. Motoba, Phys. Rev. C **97**, 064318 (2018).

[79] P. W. Zhao, Z. P. Li, J. M. Yao, and J. Meng, Phys. Rev. C **82**, 054319 (2010).

[80] F. Vogler, J. Böttcher, W. Eyrich, A. Hofmann, M. Meyer, and U. Scheib, Phys. Rev. C **28**, 1925 (1983).

[81] R. J. Vojtech, J. J. Kolata, L. A. Lewandowski, K. E. Rehm, D. G. Kovar, G. S. F. Stephans, and M. F. Vineyard, Phys. Rev. C **39**, 1377 (1989).

[82] B. Pritychenko, M. Birch, B. Singh, and M. Horoi, At. Data Nucl. Data Tables **107**, 1 (2016).